Methane dry reforming over boron nitride interface-confined and LDHs-derived Ni catalysts

Kankan Bu[a], Sanchai Kuboon[b], Jiang Deng[a], Hongrui Li[a], Tingting Yan[a], Guorong Chen[a], Liyi Shi[a], Dengsong Zhang[a,*]

[a] Department of Chemistry, College of Sciences, Research Center of Nano Science and Technology, Shanghai University, No. 99 of Shangda Road, Shanghai, 200444, PR China
[b] National Nanotechnology Center, National Science and Technology Development Agency, 111 Thailand Science Park, Pathum Thani, 12120, Thailand

ABSTRACT

Improving catalytic stability of nickel-based catalysts in terms of coking and sintering-resistance is urgent for methane dry reforming. Here, we rationally designed and originally developed an efficient and stable boron nitride interface-confined and layered double hydroxides (LDHs)-derived Ni catalysts (NiMA-BN-M-R) for methane dry reforming. It was demonstrated that the confinement derived from the interface between h-BN and LDHs-derived $(Ni,Mg)Al_2O_4$-sheets were responsible for well-dispersed Ni nanoparticles. The in situ diffuse reflectance infrared Fourier transform spectroscopy results indicate the strong CO_2 adsorption with enhancement of both CH_4 and CO_2 activation over NiMA-BN-M-R, resulting in the fast formation of carbonate and hydroxyl species which is beneficial for methane dry reforming reaction. The hydroxyl species can spontaneously react with the CH_x^* to form desired products and prevent coke formation, thus improving the stability of Ni-based catalysts. Eventually, the NiMA-BN-M-R catalyst showed excellent stability after it was employed in the reaction for 20 h and regenerated for another 100 h reaction. The confinement effect of the $h-BN/(Ni,Mg)Al_2O_4$-sheets interface and the strong metal support interaction are primary reasons for the excellent stability of the NiMA-BN-M-R catalyst. This work unlocks the development of a high thermal stability composites catalysts for methane dry reforming.

1. Introduction

Methane dry reforming (MDR) is a promising process for converting two major greenhouse gases, methane (CH_4) and carbon dioxide (CO_2), into syngas (mixture of H_2 and CO), which is beneficial for reducing global warming issues [1–3]. The produced syngas from this process can also be utilized as precursors for preparation of high value-added chemicals, such as methanol, formic acid, acetic acid, and other chemicals through Fischer-Tropsch synthesis [4]. Nevertheless, due to the high endothermicity and slow kinetics of the MDR reaction, it requires high operational temperatures of 700–900 °C [5,6]. Therefore, thermally stable catalysts are needed to ensure the effective conversion of CH_4 and CO_2 at such high temperature. Generally, precious metal catalysts show high activity in the MDR reaction. However, their industrial applications are limited due to economic reasons [7,8]. Consequently, it is particularly urgent to develop non-noble metals as MDR catalysts. Among various non-precious metals, nickel-based catalysts are preferred because of its inexpensiveness and abundance [9]. In the MDR

reaction, despite of their high activity, the nickel catalysts are suffered from sintering at high temperatures (often higher than the Tammann temperature (691 °C of Ni)) and coking formation [10]. The coking process or carbon deposition mainly occurs due to the Boudouard reaction ($2CO \rightarrow C + CO_2$) and methane decomposition ($CH_4 \rightarrow C + 2H_2$). The sintering of active species and carbon deposits can easily lead to deactivation of nickel-based catalysts [11].

In order to maintain the nickel-based catalysts' high activity and improve their stability under harsh conditions, great efforts have been made [12,13]. Coke formation during MDR is often addressed through active metal passivation by doping other elements or accelerating coke removal via optimization of Ni nanoparticle size or modification of support [14,15]. For example, metal dispersion was significantly improved by doping basic metal oxides or introducing the second metal into the nickel catalyst which is beneficial for CO_2 adsorption and activation to gasify carbon [16,17]. The Ni sintering can be suppressed though steric confinement by coating mesoporous oxides or tuning the strong metal support interaction (SMSI) [18,19]. Immobilizing nickel

---

* Corresponding author.
  E-mail address: dszhang@shu.edu.cn (D. Zhang).

nanoparticles in porous shells or construction of catalysts with metal and support core-shell structures can also help to suppress the sintering of nickel particles [20]. Moreover, it is interesting that the coking and sintering of Ni-based catalysts could be inhibited simultaneously while the high catalytic activity was still maintained by introducing defects into supports [21]. As described above, a rational design of supports would contribute to sintering resistance and coke inhibition of the catalysts.

In recent decades, layered double hydroxides (LDHs) derived transition metal oxides with adjustable metal compositions attract great interest due to their unique physical and chemical properties, such as diversity of compositions, high dispersion of metal species and plenty of basic sites [22,23]. Principally, LDHs are favorable for supported catalysts with high metal dispersion because of the homogeneous elements' distribution. Additionally, the hydroxide-to-oxide support transformation after calcination could trigger the SMSI with oxide barriers on the active nanoparticles leading to sintering-resistant at high temperatures [24]. Through adjustment of the element species and/or ratios and incorporation with porous supports, the Ni-based LDH-derived oxides with well-dispersed metal were prepared and showed sintering-resistance for MDR [25,26]. However, it is still a big challenge to achieve coking resistance and sintering tolerance at the same time.

Most recently, hexagonal boron nitride (h-BN) has attracted interest in various fields because of its unique chemical inertness, high oxidation resistance and thermal stability [27]. Regarding heterogeneous catalysis, the h-BN has shown great potential for olefin production as metal-free catalyst [28]. Through construction of the interface between Ni and h-BN, the performance of syngas methanation has been greatly improved due to the confinement effect of the top 2D covers [29]. Previously, we have constructed the Ni nanoparticles supported by h-BN with abundant vacancy defects [21] as well as supported by h-BN combining with the steric confinement by meso-SiO_2 [30] for MDR reaction. The B−OH in situ forms during reaction and dramatically reduces the coke formation. As a new strategy, we have incorporated Ni-based LDHs with h-BN in order to promote the confinement effect achieving inhibition of coking and sintering simultaneously. The interface confinement can prevent the growth of Ni nanoparticle and hence result in well-dispersed active metal. Meanwhile, the incorporation of h-BN would benefit the coking resistance.

In the present work, the h-BN interface-confined and LDHs-derived Ni catalysts were designed and originally synthesized by controlling of Ni-Mg-Al-LDHs growth on the surface of h-BN and underwent annealing process subsequently. The immobilization of the Ni nanoparticles through the confinement of the LDHs-derived $(Ni,Mg)Al_2O_4$-sheets interface contributed to the homogenously dispersed Ni nanoparticles. Meanwhile, the in situ diffuse reflectance infrared Fourier transform spectroscopy (in situ DRIFTS) results indicate the fast transformation of CH_x^* over the surface −OH sites generated on the interface of h-BN/$(Ni,Mg)Al_2O_4$ significantly suppresses carbon deposition. The chemisorption results reveal that an enhanced CO_2 adsorption induced by h-BN can promote the conversion of CH_4. Subsequently, the targeted catalyst showed very high conversion for CH_4 and robust stability with only 1% activity drop after 100 h testing. Our results demonstrate that construction of interface between LDH-derived oxides and layered materials can achieve robust stability with high reaction activity simultaneously, which is promising for the development of highly stable MDR catalysts.

2. Experiments

2.1. Catalyst preparation

2.1.1. Preparation of NiMA-BN-x-R catalysts

Firstly, the h-BN was pretreated as follow: 0.5 g commercial h-BN was dispersed in 70 mL 30 wt% hydrogen peroxide solution and magnetically stirred for one day. The mixture was later placed in a 100 mL autoclave with a Teflon liner at temperature of 120 °C for one day to attach the h-BN surface on a negatively charged hydroxyl species (as shown in FTIR spectrum in Fig. S1). Then the hydrogen peroxide solution was removed using vacuum filtration. The h-BN residue was later washed with deionized water (DI) for 3 times and dried in oven at 60 °C overnight [31]. Secondly, different amounts of pretreated h-BN were added to the aqueous solution of nickel nitrate, magnesium nitrate and aluminum nitrate with an atomic ratio of 0.86: 5.14: 2.00 (Ni: Mg: Al) and sonicated for about 12 h to ensure that the metal ions were uniformly dispersed and adsorbed on the surface of the h-BN by electrostatic action. Subsequently, 0.15 mol of sodium hydroxide solution was rapidly mixed with the as-prepared solution above under vigorous stirring. After 10–15 min, the obtained colloidal sample was washed two times with DI and gathered through centrifugation and re-dispersed in 80 mL DI. The re-dispersed sample was transferred to a 100 mL Teflon autoclave and heated at 150 °C for 15 h. Eventually, after cooling down, the rotary evaporator was used to evaporate the water while the powder sample was collected and calcined in air at 550 °C for 6 h (labeled NiMA-BN-x-O (O represents oxide)) and reduced under 10 v% H_2/N_2 atmosphere at 750 °C for 1 h (labeled NiMA-BN-x-R (R represents reduced species)). In order to obtain the best ratio of composite samples, we prepared three different nickel loadings as donated with x in the following sample named as NiMA-BN-L-R (L means the low nickel loading of 3 wt%), NiMA-BN-M-R (M means the middle nickel loading of 5 wt%), and NiMA-BN-H-R (H means the high nickel loading of 10 wt%) by adjusting the mass of h-BN added.

2.1.2. Preparation of NiMA-y-R catalysts

The preparation of NiMA-y-R catalysts were similar to the method above except without an addition of h-BN. A molar ratio of Ni: Mg: Al in the metal nitrate precursors was 0.86: 5.14: 2.00 mmol, giving the Ni loading of 14 wt% and denoted as NiMA-1-R. To maintain the same Ni loading of 5 wt% with that of the NiMA-BN-M-R catalyst described above, we prepared the LDHs precursor derived catalyst with the similar Ni loading by adjusting the molar ratio of the mixed metal nitrate (Ni: Mg: Al in a 0.34: 5.66: 3.00) mmol, which was labeled as NiMA-2-R.

2.1.3. Preparation of Ni-BN-R catalysts

A suspension containing a certain amount of h-BN and nickel nitrate was ultrasonicated at room temperature for 12 h. Then, the powdered sample was obtained using a rotary evaporator. Finally, the collected powder was calcined in air at 550 °C for 6 h and reduced under 10 v% H_2/N_2 atmosphere at 750 °C for 1 h. The obtained catalyst with 5 wt% Ni loading was denoted as Ni-BN-R.

2.1.4. Preparation of MA-O sample

The preparation of MA-O sample was similar to that of the NiMA-y-O except an addition of the Ni precursor. A molar ratio of Mg: Al in the metal nitrate precursors was 6.00: 2.00 mmol.

2.2. Catalysts characterization

Transmission electron microscopy (TEM) and high-resolution transition electron microscopy (HRTEM) images were gathered on a JEM-2010 F (JEOL, Japan) equipped with an element mapping technique. X-ray diffraction (XRD) was performed using a Rigaku D/MAX-RB X-ray diffractometer with Cu Ka radiation and scanned in the 2θ range of 10-90° with a step size of 8°min^{-1}. The size of Ni nanoparticle was calculated via Scherrer equation based on the full width at half maximum (FHWM) of the main peaks. Thermogravimetric analyses (TG) were measured on NETZSCH STA 449 F1 from 25 to 800 °C at a ramping rate of 10 °C min^{-1} under an oxidative atmosphere to analyze the weight of coke on the spent catalysts. Nitrogen adsorption-desorption measurements were performed on an Autosorb-iQ2 (Quantachrome). Specific

surface areas (SSA) were calculated by the Brunauer-Emmett-Teller (BET) equation. The basicity of the catalysts was analyzed by the CO_2 temperature-programmed desorption (CO_2-TPD). Before the TPD test, 0.080 g fresh catalysts were heated at 300 °C for 30 min under He flow (30 mL·min^{-1}). When it cooled to 50 °C, a 30 mL min^{-1} CO_2 gas flow was introduced for 1 h. After that, the physical absorbed CO_2 was removed using He flow for 30 min. Then, the catalysts were heated in a He flow from 50 to 750 °C at the heating rate of 10 °C min^{-1}. H_2-temperature programmed reduction (H_2-TPR) measurements were carried out on a fixed-bed reactor. Before reduction, 0.080 g powered were heated at 300 °C for 30 min with nitrogen flow (30 mL·min^{-1}). After cooling to 25 °C, a 30 mL min^{-1} 10% H_2/N_2 mixture gas flow was introduced to the sample and heated from 25 °C to 900 °C (10 °C min^{-1}). The CO_2-TPD and H_2-TPR were both tested by a quartz tube reactor equipped with a thermal conductivity detector (TCD).

The Micromeritics AutoChem II 2920 was used to detect Ni dispersion of the catalysts by H_2 pulse chemisorption. Firstly, the catalysts were reduced at 750 °C for 1 h under a 10% H_2/Ar flow (30 mL·min^{-1}), and then cooling down to 50 °C under Ar stream (30 mL min^{-1}). Next, H_2 pulses were injected until the eluted peak area of consecutive pulses remained stable.

In situ diffuse reflectance infrared Fourier transform spectroscopy (in situ DRIFTs) experiments was measured on a Nicolet 6700 spectrometer with a mercury-cadmium-telluride detector and the resolution is 4 cm^{-1}. For all the DRIFTs experiments, the catalysts were firstly purged with N_2 at 300 °C for 30 min and the flow rate was 50 mL min^{-1}. In the transient experiment studies, the catalysts were exposed to CO_2 (40 mL min^{-1}) at 500 °C for 1 h. And then switching the gas to CH_4 (40 mL min^{-1}), and the spectra were collected. Moreover, to understand the reaction mechanism, we also collected the spectra during the MDR reaction in the temperature maintained at 500 °C and the temperature between 400–700 °C with a 50 °C step ($CH_4/CO_2/N_2$ = 10/10/50 mL/min).

2.3. Catalytic tests

For an MDR reaction, 0.12 g catalyst powder was loaded in a tubular quartz reactor (10 mm × 1 mm × 285 mm) before CH_4 and CO_2 gas mixture (CH_4/CO_2 = 25/25 mL·min^{-1}) was introduced. Later, a reaction temperature was ramped to 750 °C and maintained for 20 h for typical catalytic testing. In addition, stability evaluation of selected catalysts in the MDR reaction was tested at 750 °C for 100 h. Gas products and reactants were analysed using gas chromatograph (GC, 9890 A, linghuayiqi) equipped with a TCD detector.

3. Results and discussion

3.1. Characteristics

3.1.1. Morphology analysis

The morphology and structural properties of the reduced NiMA-BN-M-R catalyst were investigated. As shown in Fig. 1(a), the (Ni,Mg)Al$_2$O$_4$-sheets were grown well on the surface of h-BN, while metallic nickel nanoparticles are evenly dispersed and embedded in the (Ni,Mg)Al$_2$O$_4$-sheets. The Ni particle size is mainly distributed between 8–10 nm and the average particle size is 9.6 nm (estimated by TEM). When compared with other contrast samples (Table 1 and Fig. S4), the NiMA-BN-M-R had the smallest Ni particles. Simultaneously, the highest Ni dispersion (14.46%) of NiMA-BN-M-R (Table 3) suggested the well-dispersed Ni, which is consistent with the TEM results. The lattice fringes spacing is 0.206 nm (Fig. 1(b)), corresponding to the (111) plane of metallic Ni. Through the cross-sectional analysis along with the EDX line scan in SEM, we can see that the (Ni,Mg)Al$_2$O$_4$-sheets were well combined with h-BN layer by layer (Fig. 1c and Fig. S2). Additionally, the nickel particles in the NiMA-BN-x-R and NiMA-y-R catalysts were also dispersed uniformly. On the contrary, the nickel

particle size in Ni-BN-R catalyst was significantly larger than that of confined catalysts (Fig. S3). It is obvious that the confinement strategy contributes to smaller Ni nanoparticle (Fig. S3(b)). Furthermore, the spatial distribution of elements contained in the catalysts were confirmed by EDX analyses, further revealing the high dispersion of nickel particles with small nanometer size with the LDHs assisting dispersion and interface confinement (Fig. 1(d)). The morphology analysis proved that the confinement effect derived from the h-BN/(Ni,Mg)Al$_2$O$_4$-sheets interface could prevent the aggregation of Ni during the high temperature treatment.
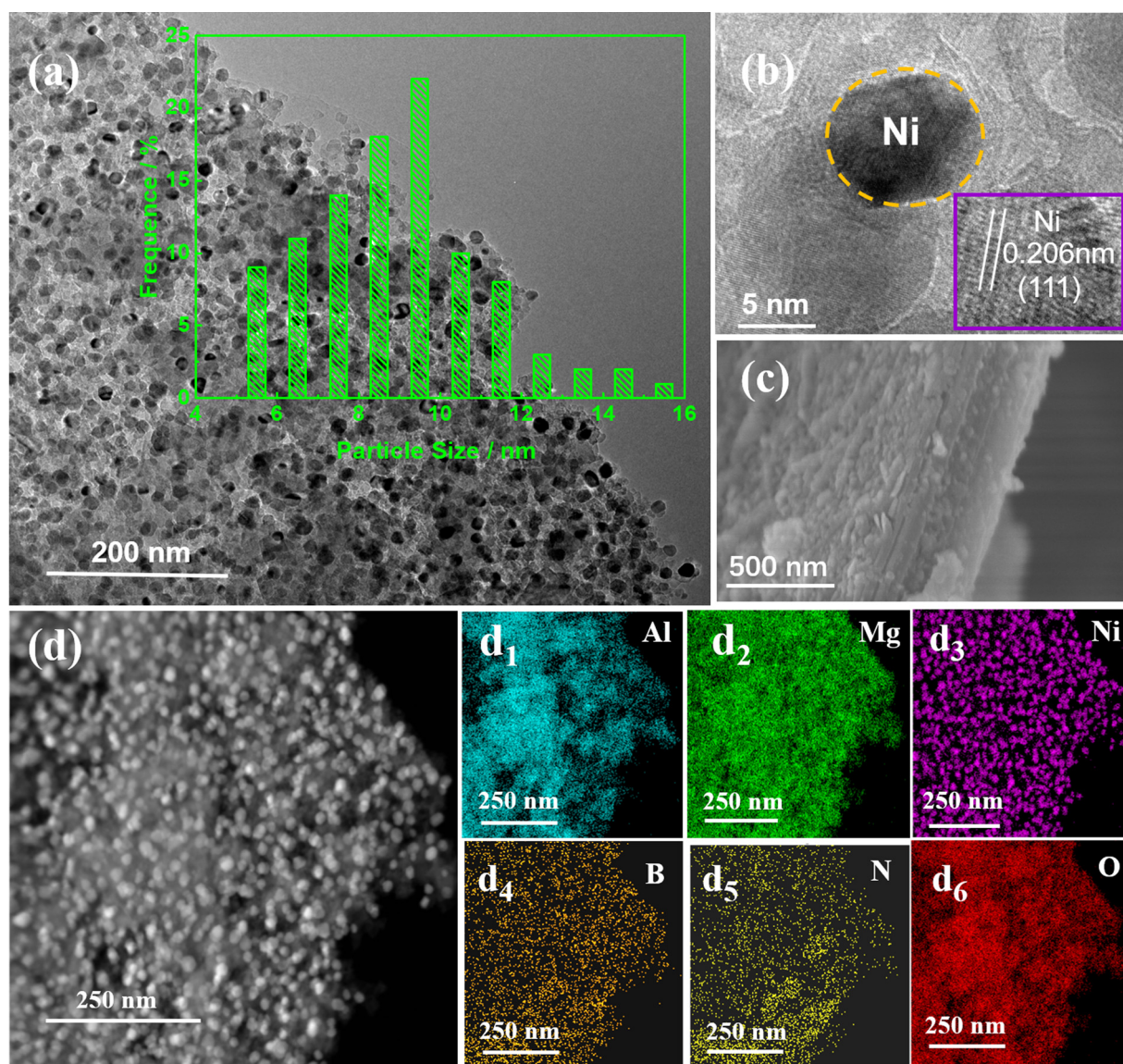
3.1.2. Structural properties

Fundamental structural characterizations of all samples were performed using XRD. Fig. 2(a) showed the XRD patterns of the prepared NiMA-BN-x-O and NiMA-y-O serial samples with varying Ni loadings and Ni-BN-O samples. Both NiMA-BN-x-O and NiMA-y-O samples displayed diffraction peaks belonged to (Ni,Mg)Al$_2$O$_4$ periclase phase, NiAl$_2$O$_4$ (JCPDF no. 10-0339), MgAl$_2$O$_4$ (JCPDF no. 21-1152), suggesting that nickel was incorporated into the periclase phase. In addition, NiMA-BN-x-O also had the diffraction peaks of h-BN phase (JCPDF no. 34-0421). Because of the high degree of crystallinity for h-BN, the diffraction peaks of h-BN phase were evident [26]. The Ni-BN-O samples showed the diffraction peaks of NiO phase and the h-BN phase [32,33]. Fig. 2 (b) represented XRD patterns of samples after reduction which obviously showed that all samples were remained in the (Ni,Mg)Al$_2$O$_4$ periclase phase except the Ni-BN-R even at the high reduction temperature of 750 °C. Meantime, the diffraction peaks of NiO disappeared, indicating the successful reduction of Ni^{2+} to Ni^0 at 750 °C [34]. However, it was difficult to distinguish the diffraction peaks of Ni^0 because of the small loading (~ 3%) and overlaying with diffraction signal of h-BN for the NiMA-BN-L-R. For the NiMA-BN-x-R samples, the intensity of the diffraction peaks belong to h-BN increases with higher h-BN mass ratio (Fig. S5). A summary of specific surface area (SSA) for all samples was given in Table 1. The SSA values diminished with increasing of h-BN content due to the smaller SSA of h-BN. XRD results showed that the Ni species were successfully incorporated into the (Ni,Mg)Al$_2$O$_4$-periclase framework. The average Ni particle size was calculated through the Scherrer equation, the results were very similar to those of TEM statistics (Fig. 1(a) inset and Table 1). Meanwhile, the morphology analysis of the catalysts also proved that the (Ni,Mg)Al$_2$O$_4$-sheets grew on the surface of h-BN, which provided credible evidences for the confinement structure of NiMA-BN-M-R catalysts.

3.1.3. H_2-TPR and XPS analysis

The H_2-TPR was used to study the redox properties of all the calcined samples. There is no reduction peak over MA-O (derived from the Mg, Al-LDHs), which means the MgO$_x$ or AlO$_x$ cannot be reduced under this condition (Fig. 3(a)). While for the NiMA-BN-M-O catalyst, as shown in Fig. 3(a), the temperature range of reduction peak was observed at 658~833 °C, and for NiMA-BN-L-O, NiMA-BN-H-O, NiMA-1-O and NiMA-2-O, the temperature range of reduction peak was observed at 647–821 °C, 612–869 °C, 403–529 °C and 588–874 °C, 398–554 °C and 606–884 °C respectively. For the Ni-BN-O catalyst, the reduction peaks could be observed at 404~562 °C, which could be divided into three reduction peaks, indicating the inhomogeneous particle size distribution. The reduction peaks at lower temperature (below 562 °C) could be attributed to the reduction of the isolated bulk NiO on the outside of the (Ni,Mg)Al$_2$O$_4$ periclase framework to metallic nickel, indicating a weak metal carrier interaction [35]. The reduction peaks at higher temperature (above 588 °C) could be ascribed to the reduction of the Ni^{2+} in the (Ni,Mg)Al$_2$O$_4$ periclase framework to metallic nickel. This may be due to the SMSI between nickel and the formed (Ni,Mg)Al$_2$O$_4$ periclase [36]. Combining with the XRD results, it could be proved that the reduction peak at higher temperature was mainly attributed to NiAl$_2$O$_4$. For all the NiMA-BN-x-O samples, there was only one reduction peak, belonging to the reduction of Ni^{2+} to Ni° [37]. In

Fig. 1. (a) TEM image with the size distributions of Ni particles (inset); (b) HRTEM image; and (c) SEM image and (d) elemental mapping results for the NiMA-BN-M-R catalyst.

Table 1
Average nickel particle size and BET specific surface area for all the samples.
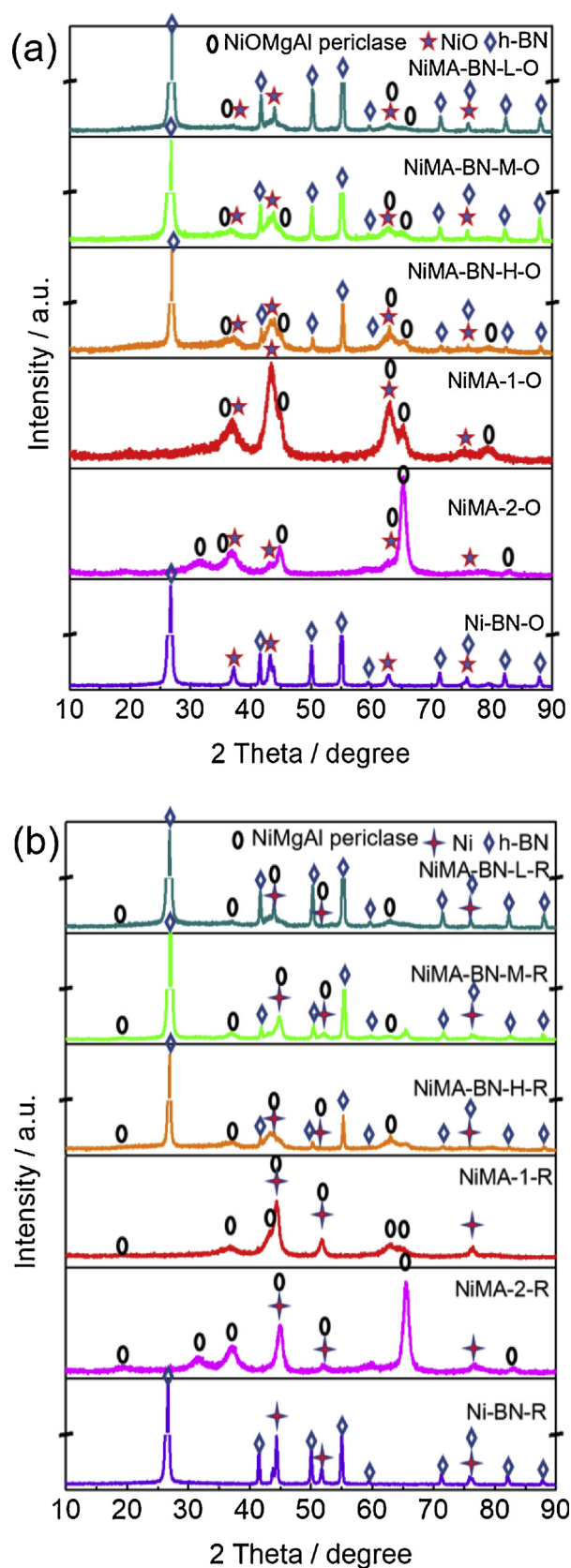
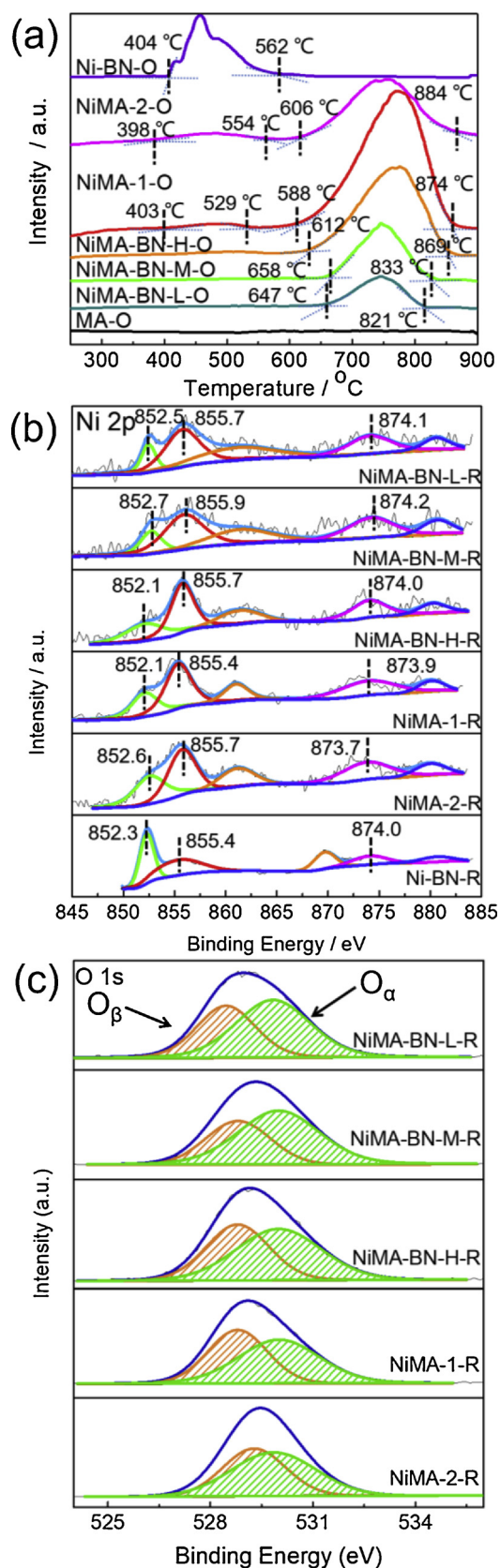| Catalysts	Average size of Ni particles / nm						BET SSA/m^2 g^{-1}	
	Fresh		Spent				Fresh	Spent[c]
	a	b	a		b			
NiMA-BN-L-R	12.69	12.86	16.87[c]		17.46 [c]		14	8
NiMA-BN-M-R	9.60	11.09	11.73[c]	12.54[d]	12.79[c]	13.53[d]	20	12
NiMA-BN-H-R	13.16	15.98	24.21[c]		22.47[c]		76	19
NiMA-1-R	15.41	15.19	29.16[c]		25.77[c]		123	65
NiMA-2-R	12.48	11.29	27.35[c]		24.57[c]		71	32
Ni-BN-R	20.24	21.37	30.24[c]		29.66[c]		7	4

[a] Estimated by TEM.
[b] Calculated by the Scherrer equation.
[c] The spent catalysts are obtained after the 20 h MDR reaction.
[d] The spent catalysts are obtained after the 100 h MDR reaction.

Fig. 2. XRD patterns of (a) the NiMA-BN-x-O and NiMA-y-O serial samples with varying Ni loadings and Ni-BN-O sample and (b) the NiMA-BN-x-R and NiMA-y-R serial catalysts with varying Ni loadings and Ni-BN-R catalyst.

Fig. 3. (a) H_2-TPR profiles; (b) Ni 2p and (c) O 1 s XPS spectra of the reduced catalysts.

addition, it was worth noting that the NiMA-BN-M-O showed the highest initial reduction temperature and the narrowest reduction peak temperature window of all the samples. This might be due to the SMSI. Typically, the SMSI can effectively keep the nickel species from moving under high reaction temperature, thereby preventing Ni agglomeration. In addition, the narrowest reduction peak temperature window may be due to the smallest Ni particle size [19]. When compared the NiMA-BN-x-O with NiMA-y-O, we can find that all NiMA-BN-x-O samples showed higher reduction temperature than NiMA-y-O. This means that the construction of confinement structure for the catalyst can enhance the interaction between metal and support, preventing metal sintering during the MDR reaction. The different reduction behavior of NiMA-BN-x-O can be attributed to the different interface between (Ni,Mg)Al$_2$O$_4$-nanosheets and h-BN. The suitable reduction behavior of NiMA-BN-M-O can further prove that it has the optimum interface between (Ni,Mg)Al$_2$O$_4$-nanosheets and h-BN.

The X-ray photoelectron spectroscopy (XPS) was used to determine oxidation states and chemical environment of elements on the catalyst surface. In Fig. 3(b), the spectrum of the Ni among different catalysts can be divided into two spin-orbit components, named as 2p$^{1/2}$ and 2p$^{3/2}$, respectively [34]. For all catalysts, Ni 2p$^{1/2}$ BE was ranged from 870 to 878 eV, the Ni 2p$^{3/2}$ BE was ranged from 850 to 860 eV. The peaks at around 852 eV can be attributed to metallic Ni [38]. In addition, the peaks at around 855 and 874 eV are characteristics of Ni^{2+} species. According to the literature, the BE which centered at around 855.7 eV was close to the theoretical value for the nickel aluminate phase (856.0 eV) [39]. Therefore, we assume that the existence of Ni^{2+} could be either from the oxidation of metallic Ni when exposed to air or from NiAl$_2$O$_4$ phase. Obviously, in the Ni-2p XPS spectrum, the NiMA-BN-M-R showed the highest BE (Table 2). The higher BE values may suggest the stronger metal-support interaction [14]. This can further improve the sintering resistance of the catalyst. Additionally, as is shown in Fig. S6, the BE for B 1 s and N 1 s in the NiMA-BN-M-R shifted to higher value compared with Ni-BN-R while the BE for Mg 1 s and Al 2p moved to low value compared with NiMA-1-R. It indicated the well interaction between h-BN and (Ni,Mg)Al$_2$O$_4$-nanosheets and the B and N could denote electron to Mg and Al.

The O1 s XPS spectra presented in Fig. 3(c) displayed two main peaks labelled as O$_\alpha$ and O$_\beta$. The first peak at lower BE can be assigned to the O^{2-} ions which was assumed as the lattice oxygen. The higher BE is assigned to the surface adsorbed oxygen species [40]. A summary of the quantification of corresponding proportions of the O$_\alpha$ is reported in Table 2. It showed that the NiMA-BN-x-R catalysts had a higher ratio of O$_\alpha$/O compared with the NiMA-y-R catalysts. Moreover, the O$_\alpha$/O ratio of the NiMA-BN-M-R catalyst has the highest value. Compared with the O$_\beta$, the O$_\alpha$ is more reactive toward oxidizing carbon species, which can help to eliminate coke deposition and suppress the deactivation of the catalyst during the MDR reaction [41,42].

3.1.4. CO$_2$-TPD analysis

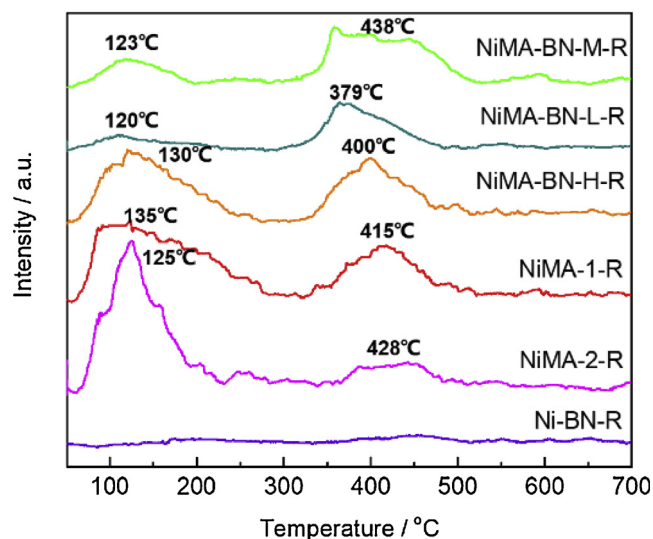The basicity of the catalysts is important for adsorption and

Table 2
Oxidation states and chemical environment of elements on the catalyst surface from XPS analysis.

Catalysts	Binding energy and concentration of O$_a$			
	Ni 2p$^{3/2}$ (eV)		Ni 2p$^{1/2}$ (eV)	O$_a$/O (%)
	Ni°	Ni^{2+}		
NiMA-BN-L-R	852.5	855.7	874.1	58.86
NiMA-BN-M-R	852.7	855.9	874.2	62.93
NiMA-BN-H-R	852.1	855.7	874.0	55.51
NiMA-1-R	852.1	855.4	873.9	53.94
NiMA-2-R	852.6	855.7	873.7	54.96
Ni-BN-R	852.3	855.4	874.0	–

Fig. 4. CO$_2$-TPD profiles of all the fresh catalysts.

activation of CO$_2$ to produce CO. The reactive oxygen species generated by CO$_2$ activation can help to eliminate the coke formation [43]. Here, CO$_2$-TPD was used to study the basicity of the catalysts. As shown in Fig. 4, two broad adsorption peaks at approximately 125 and 415 °C were observed in all reduced samples except the Ni-BN-R catalyst. It is generally considered that the peak at lower temperature can be ascribed to the weak basic sites corresponding to the physical adsorption of CO$_2$. The peak appearing at the high temperature corresponds to the strong basic sites due to the chemisorption of CO$_2$. And the larger the peak area, the higher numbers of basic sites are presented in the catalyst [44]. In addition, many studies have suggested that the SSA of the catalyst has a great influence on the CO$_2$ adsorption capacity of the catalyst [44]. It was found that there were no obvious CO$_2$ desorption peaks over Ni-BN-R, indicating that there were few adsorbed reactant molecules for the Ni-BN-R catalyst at the reaction temperature (Fig. 4). For NiMA-BN-x-R, the peak area in the lower temperature diminished with the increase of h-BN content due to its smaller SSA. At the same time, the NiMA-BN-M-R showed the highest desorption temperature and a larger amount of CO$_2$ desorption at high temperature because of the optimum interface between the (Ni,Mg)Al$_2$O$_4$-sheets and h-BN. Combined with the XPS results (Fig. S6), the optimum interface between the (Ni,Mg)Al$_2$O$_4$-sheets and h-BN is beneficial for the electrons transferring from B, N to Mg, Al, thus improving the alkalinity of the catalyst and enhancing the adsorption and activation of CO$_2$. At low temperature, the NiMA-y-R showed a larger amount of CO$_2$ desorption due to its larger SSA (Table 1). It is clear that an appropriate interface between (Ni,Mg)Al$_2$O$_4$-sheets and h-BN results in an increase of strong basic sites, which may favor the MDR reaction.

3.2. Catalytic performance

All the reduced catalysts were tested for the MDR reaction under a specific reaction condition (WHSV = 25,000 mL^{-1} g$_{cat}$$^{-1}$ h^{-1}, CH$_4$: CO$_2$ = 1: 1, ambient atmosphere) at 750 °C for 20 h. The stability curves of all catalysts with time on stream were shown in Fig. 5. It was found that the NiMA-1-R and the NiMA-BN-H-R catalysts showed higher initial CH$_4$ and CO$_2$ conversions due to the higher loading of Ni species. Similar initial conversion of CH$_4$ was found for the NiMA-BN-M-R and the NiMA-2-R with the same loading of Ni species. The NiMA-BN-L-R showed a lower initial CH$_4$ and CO$_2$ conversions, which may be due to relatively fewer active sites with lower Ni loading [9]. The lowest initial CH$_4$ and CO$_2$ conversions happened to the Ni-BN-R, which can be attributed to the low dispersion of nickel species (Table 3) [45,46]. The CH$_4$ conversion of all samples, except the NiMA-BN-M-R,
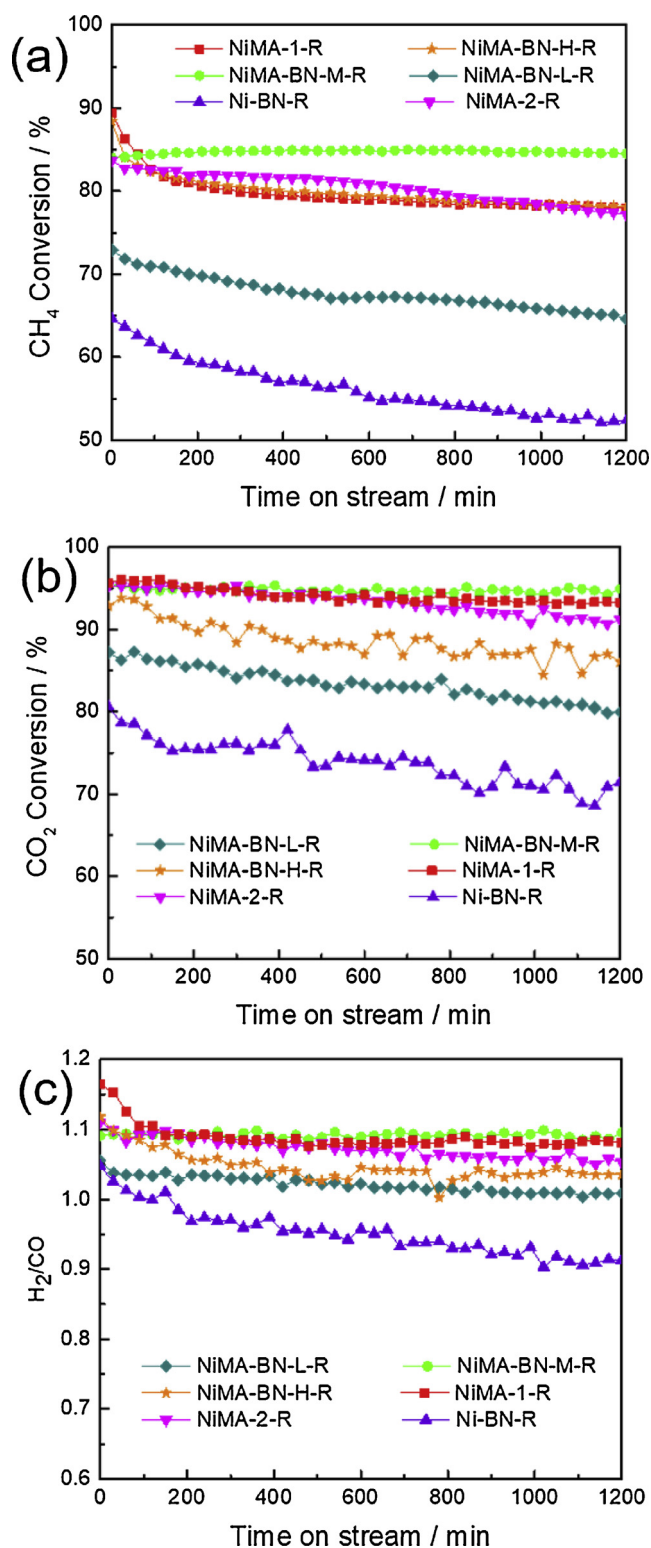
Fig. 5. (a) CH_4 and (b) CO_2 conversion as a function of time on stream and relevant (c) H_2/CO ratio over the reduced catalysts.

decreased gradually with the continual MDR reaction, which may be due to the agglomeration of the nickel species or the coke covering the nickel active site during the reaction. For the NiMA-BN-M-R catalyst, the CH_4 and CO_2 conversions remained almost unchanged after the 20 h MDR reaction (Fig. 5(a) and (b)). Instead, for other catalysts, the CH_4 conversions decreased significantly in the 20 h MDR reaction. For NiMA-1-R, NiMA-BN-H-R, NiMA-BN-L-R, NiMA-2-R and Ni-BN-R

catalysts, the CH_4 conversions decreased about 11%, 10%, 8%, 7%, and 12%, respectively. In addition, the turnover frequency (TOF) of CH_4 defined as CH_4 conversion per surface Ni atom per second, was calculated by estimating Ni dispersion of the catalysts by H_2 pulse chemisorption to compare the reaction activity [47]. The NiMA-BN-M-R has the highest activity ($TOF_{CH4} = 2.18\ s^{-1}$) due to more reactive sites derived from high metal dispersion (Table 3 and Fig. S7). The difference of carbon deposition and metal sintering among various catalysts may result in dissimilarity in catalyst stability [26]. The stability test results proved that an addition of appropriate amount of h-BN can contribute to the tolerance for MDR reaction. The h-BN, because of the thermostability, can effectively inhibit the agglomeration of the oxide sheets, thereby preventing the Ni sintering and hence helping to maintain the catalytic durability against metal sintering. This also can be proved by the TEM and the Ni dispersion of the spent catalysts (Fig. S9 and Table S1).

In Fig. 5(b), the conversion of CO_2 is relatively higher than that of CH_4 in all catalysts. This indicated the presence of reverse water-gas shift (RWGS) reaction [16,48]. Moreover, H_2/CO ratio can further reflect the selectivity of the catalyst. For almost all catalysts, the mole ratio of H_2/CO is slightly higher than 1 and gradually decreased with the increase of reaction time. This may be due to the decomposition of methane to produce H_2 and carbon, thereby increasing the ratio of H_2/CO (Fig. 5 (c)) [49]. The reduced H_2/CO ratio can be attributed to the coke covering the active sites during the MDR reaction, which leads to the inhibition of CH_4 decomposition and finally results in the difference of activity decays. But for the NiMA-BN-M-R catalyst, the H_2/CO ratio is maintained. This can further illustrate that the NiMA-BN-M-R catalyst had good stability in MDR reaction.

To prove the superior stability of NiMA-BN-M-R, an MDR reaction was further conducted for 100 h over this catalyst (Fig. 6). The NiMA-BN-M-R catalyst displayed excellent stability during the 100 h MDR reaction. In addition, in order to evaluate the recyclability of the NiMA-BN-M-R catalyst, we also regenerated and tested the performance of this catalyst. The spent NiMA-BN-M-R catalyst after 20 h MDR reaction were re-oxidized to remove the coke, and reduced in hydrogen atmosphere then reused for another 100 h MDR reaction (Fig. S8). The refreshed NiMA-BN-M-R catalysts showed good stability even after 100 h for repeated testing (Fig. S8). The excellent catalytic regeneration stability of NiMA-BN-M-R will make it promising for the industry application.

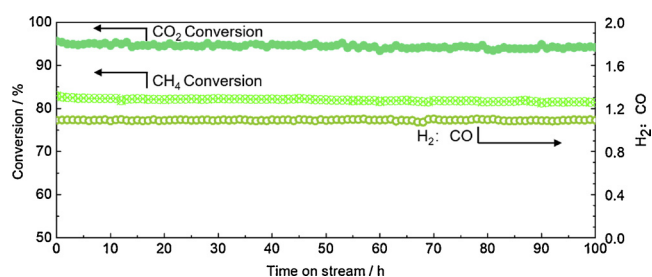### 3.3. Characteristics of the spent catalysts

TEM images of the spent catalysts are depicted in Fig. S9 and Fig. S11. The average nickel particle size and its size distributions after reaction were also given in Table 1, Fig. S10 and Fig. S11. The Ni particles of the spent NiMA-BN-M-R still maintained good dispersion and the average size is about 13 nm even after 100 h MDR reactions. The good resistance to metal sintering can be attributed to the SMSI and interface confinement effects [50]. For the other samples, the larger Ni particle size and filamentous carbon (Fig. S9, Fig. S11 and Table 1) after the MDR reaction is responsible for the inactivation of the NiMA-BN-L-R, NiMA-1-R, Ni-BN-R, NiMA-2-R and NiMA-BN-H-R.

The catalysts' SSA before and after the 20 h MDR reaction (750 °C, with total gases flowing of 50 ml/min CH_4: $CO_2 = 1$: 1) were also summarized in Table 1. The Ni dispersion before and after 6 h MDR reaction (550 °C, with a total gas flow of 90 ml/min CH_4: $CO_2 = 1$: 1) were summarized in Table 3. Compared with the fresh catalysts, the SSA of NiMA-1-R decreased significantly after the MDR reaction, while Ni dispersion of NiMA-BN-M-R decreased slightly. This further proved that the addition of h-BN can prevent the collapse of (Ni,Mg)Al_2O_4-sheets, thereby inhibiting Ni sintering.

The XRD patterns (Fig. S12) of the samples after MDR reaction showed that there was almost no change in crystal structure and crystalline phases except a wide carbon peak around 25-26° compared with the fresh NiMA-1-R and NiMA-2-R catalysts. The strong carbon peak

Table 3
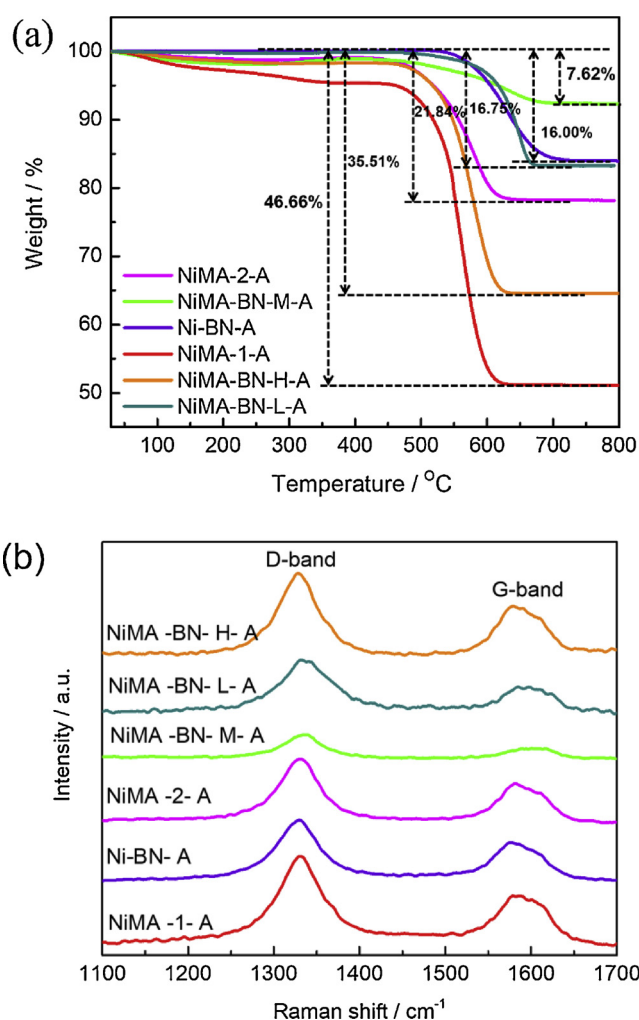The Ni dispersion and the TOF$_{CH4}$ of the as-prepared catalysts during the DRM reaction at 550 °C.

Catalysts	Loading of Ni (wt%)[a]	H$_2$ adsorption (µmolg$_{cat}^{-1}$)[b]		Ni dispersion[c] (%) H$_2$ adsorption (H/Ni)		TOF$_{CH4}$[d] (S^{-1})	
		t = 0 min	t = 360 min	t = 10 min	t = 360 min	t = 10 min	t = 360 min
NiMA-BN-M-R	2.84	34.99	33.51	14.46	13.85	2.18	2.03
NiMA-BN-ʟ-R	2.15	22.84	16.87	12.47	9.21	0.86	0.61
NiMA-BN-H-R	10.32	67.00	47.48	7.62	5.40	0.64	0.63
NiMA-1-R	17.44	112.77	52.60	7.59	3.54	0.57	0.51
NiMA-2-R	7.63	80.47	51.87	12.38	7.98	0.60	0.57
Ni-BN-R	4.64	7.71	4.86	1.95	1.23	0.39	0.33

[a] Loading of Ni was obtained by inductively coupled plasma-atomic emission spectrometer (ICP-AES).
[b] H$_2$ adsorption at 50 °C.
[c] Ni dispersion were measured by H$_2$ pulse chemisorption.
[d] The value of TOF was tested at 550 °C with CH$_4$ flowing of 45 ml/min.

Fig. 6. CH$_4$ and CO$_2$ conversion as a function of time on stream and relevant H$_2$/CO ratio over the NiMA-BN-M-R catalysts for 100 h.

indicates the presence of large amount of carbon over the NiMA-1-R and NiMA-2-R causing catalyst deactivation. Meanwhile, the similar peak cannot be observed on the other catalysts owing to the high degree of crystallinity for h-BN [32]. In addition, the peak at 26° of the spent catalysts become broader than that of the fresh ones (Fig. S13), which may be due to the coke on the surface of spent catalysts. The peak intensity at 45° belonging to Ni(111) has hardly changed (Fig. S13), but the FWHM slightly decreased. The FWHM value of NiMA-BN-M-R, NiMA-BN-M-A (20 h), and NiMA-BN-M-A (100 h) was 0.766, 0.664 and 0.629, respectively. It may be attributed to slight metal sintering during high temperature reaction. Nevertheless, the NiMA-BN-M-A has the best sintering resistance ability even after the 100 h MDR reaction compared to the contrast samples (Table 1), which demonstrated that the confinement strategy used here inhibited the further growth of Ni nanoparticles.

The TG analysis was used to analyze the amount of coke formation over the spent catalysts. Generally, activated carbon species produced by the decomposition of methane are easily gasified and converted to CO, and excessive carbon species are deposited on the catalyst. Thus, the carbon deposition is generally the result of the formation and gasification equilibrium of activated carbon. In addition, the smaller Ni particle size can suppress the nucleation and growth of coke [46]. As shown in Fig. 7(a), the weight loss of NiMA-BN-L-R, NiMA-BN-H-R, NiMA-1-R, NiMA-2 and Ni-BN-R catalysts is 16.75%, 35.51%, 46.66%, 21.84% and 16.00%, respectively. While, the minimal weight loss of the NiMA-BN-M-R was presented, which is around 7.62%, proving that the best carbon deposition resistance. Even after 100 h MDR reaction, the amount of carbon deposited in NiMA-BN-M-R was significantly less than that of the NiMA-1-R for only 20 h MDR reaction (Fig. S15). TG results further indicate that the coke-resistance of the NiMA-BN-M-R can be enhanced by the small sized Ni particles and the confinement effect between (Ni,Mg)Al$_2$O$_4$-sheets and h-BN, which is agreement with the TEM results.

The structure and crystallite size of the coke on the surface of the spent catalysts can be studied by Raman spectroscopy. In Fig. 7(b), there are two peaks at around 1330 and 1581 cm^{-1} appeared for all the

Fig. 7. (a) TG profiles and (b) Raman spectra of the spent catalysts after the 20 h stability test.

spent catalysts after the 20 h MDR reaction. The peaks at 1330 cm^{-1} and 1581 cm^{-1} can belong to D-band and G-band, respectively [46,51]. The D-band represents the disordered structure of defect-rich carbon. This type of carbon is more reactive under the MDR reaction and is more easily vaporized during the reaction. The G-band reflected the ordered and well-graphitized sp^2 carbon in graphitic material, and the crystal size of carbon determines the strength of the band [7,52].

The intensity ratio of D- and G-bands (I$_D$/I$_G$) is a useful parameter to provide the information about the index of disordered and ordered carbons on the spent samples. The calculated I$_D$/I$_G$ values were

Table 4
Raman analysis of various catalysts.

Samples	I_D/I_G	I_G/I_D	Crystallite size of graphitic carbon (nm)[a]
NiMA-BN-L-A	2.01	0.49	2.16
NiMA-BN-M-A	2.67	0.39	1.72
NiMA-BN-H-A	1.73	0.58	2.55
NiMA-1-A	1.72	0.58	2.57
NiMA-2-A	1.58	0.63	2.79
Ni-BN-A	1.55	0.62	2.74

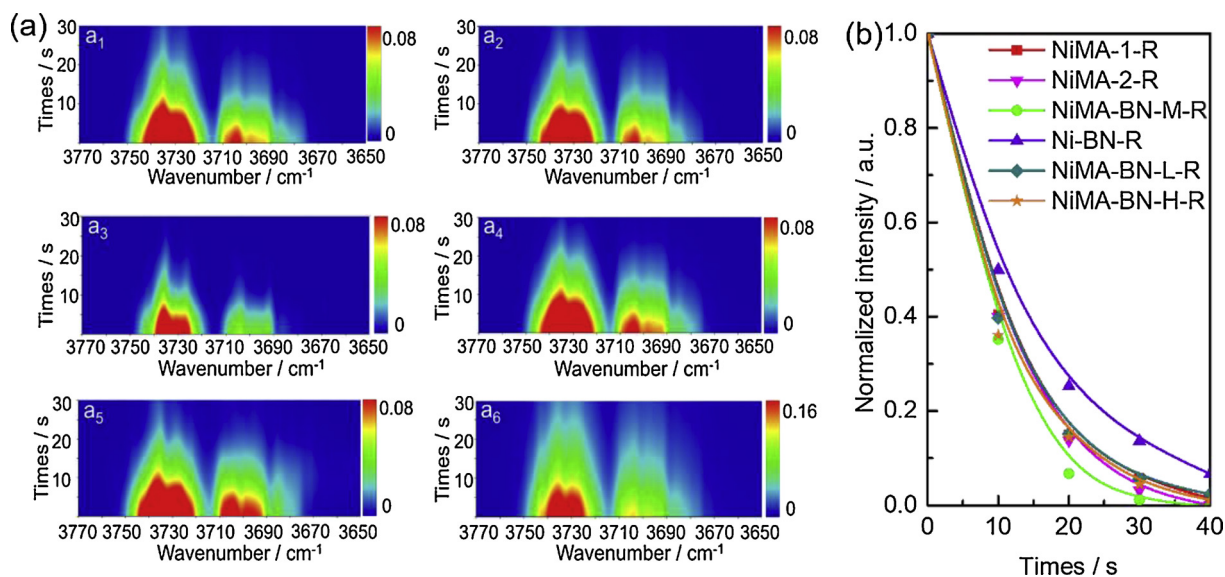[a] Calculated by the formula: Crystal size (nm) = 4.4 [I_G/I_D].

summarized in Table 3. It can be seen that the I_D/I_G values for the spent catalysts after the 20 h MDR reaction were 2.67, 1.55, 1.58, 1.72, 2.01 and 1.73 for NiMA-BN-M-A, Ni-BN-A, NiMA-2-A, NiMA-1-A, NiMA-BN-L-A and NiMA-BN-H-A, respectively. The crystal size of graphitic carbon was calculated according to a reported method and summarized in Table 4 [53]. As it can be seen from the Table 4, the graphitic carbon on the surface of NiMA-BN-M-A has the lowest graphitization degree and the smallest crystal size, indicating the limitation of carbon crystal growth over this catalyst which is related to its excellent stability. In general, the smaller crystal size of the graphitic carbon, the easier it is to be gasified with carbon dioxide to produce carbon monoxide, prolonging the life time of catalyst [6]. The results were consistent with TEM and TG analysis of the spent catalysts.

Through the above evidences on physical and chemical properties and catalytic performance analysis, the construction of optimal interface between h-BN and (Ni,Mg)Al$_2$O$_4$-sheets was briefly emphasized as the effective strategy as follows: (1) the confinement of the interface and enhanced interaction between metal and supports improves the sintering resistance of Ni particles; (2) the content of surface active oxygen, which can help to eliminate the coke on the surface of catalyst, has increased; (3) the number of strong basic sites has increased, which can improve the ability for the adsorption and activation of CO$_2$; (4) the graphitization degree of coke deposition has decreased, which means that the coke on the surface of NiMA-BN-M-R was easy to remove. Therefore, the NiMA-BN-M-R showed the best sintering resistance and excellent catalytic performance.

3.4. In situ DRIFTs study and possible reaction mechanism

In situ DRIFTs was used to explore the reaction mechanistic information about the MDR reaction over the catalysts. As shown in Fig. 8a, after the introduction of CH$_4$ over the pre-adsorbed catalyst with CO$_2$, the peaks of −OH at 3680-3750 cm^{-1} over all the catalysts decrease rapidly while exposing to CH$_4$. This means that the −OH species is involved in the MDR reaction [54]. Remarkably, the intensity of −OH over NiMA-BN-M-R is the strongest among all the catalysts and the consumption rate of −OH is the rapidest (Fig. 8b and Fig. S16). Possibly, the NiMA-BN-M-R catalyst has more nano-sized Ni particles that can provide more active sites for the activation of CH$_4$ to produce the CH$_x^*$ species. Subsequently, the active CH$_x^*$ species can react with −OH species and then transform to CH$_x$O*. The fast decrease of −OH means the rapid reaction of −OH species with CH$_4$. It can also contribute to the transformation of active carbon species and suppress the coke formation which lead to the improvement of catalyst stability [55].

To understand the catalytic reaction mechanism more incisively, the NiMA-BN-M-R catalyst was further studied by in situ DRIFTs. In Fig. 9(a) and Fig. S17, the in situ DRIFTs results could provide more information about the forms of CO$_2$ adsorption. There were two mainly adsorption forms of the CO$_2$ for the reduced catalyst. The shoulders at 1520-1550 cm^{-1} and 1625-1756 cm^{-1} belonged to the monodentate carbonates and bidentate carbonates, respectively [56]. The peaks intensity decreases with the increase of temperature, which may be due to the partial decomposition of the carbonates. At 500 °C, the characteristic peaks of the two carbonates species still are not completely disappeared, indicating that the NiMA-BN-M-R catalyst has a good adsorption and activation ability for CO$_2$, which is consistent with the CO$_2$-TPD results. In Fig. 9(b), the shoulders at 3015 and 1304 cm^{-1} corresponded to the gas CH$_4$, the shoulders at 2360 and 2340 cm^{-1} corresponded to the CO$_2$. In addition, as the reaction temperature increased, the characteristic peaks of gaseous CO appeared at 2170 and 2130 cm^{-1}. The peaks at 1625-1756 cm^{-1} and 3680-3750 cm^{-1} correspond to bidentate carbonates and −OH species indicates that the −OH and bidentate carbonates species are the main reaction intermediates [18,57–59]. At the same time, the higher reaction temperature, the stronger the CO, −OH and bidentate carbonates peaks intensity, indicating the better activity of catalyst at higher temperature. As shown in Fig. 9(c), the peaks at 1358, 1375–1590, and 1665 cm^{-1}

Fig. 8. Evolution of in situ DRIFTs after CO$_2$ adsorption at 500 °C. In situ DRIFTs of transient reactions over a) over the reduced catalysts (a$_1$ is the NiMA-BN-L-R, a$_2$ is the NiMA-BN-H-R, a$_3$ is the NiMA-BN-M-R, a$_4$ is the NiMA-2-R, a$_5$ is the NiMA-1-R and a$_6$ is the Ni-BN-R); (b) consumption of −OH species upon passing CH$_4$ stream over the reduced catalysts.
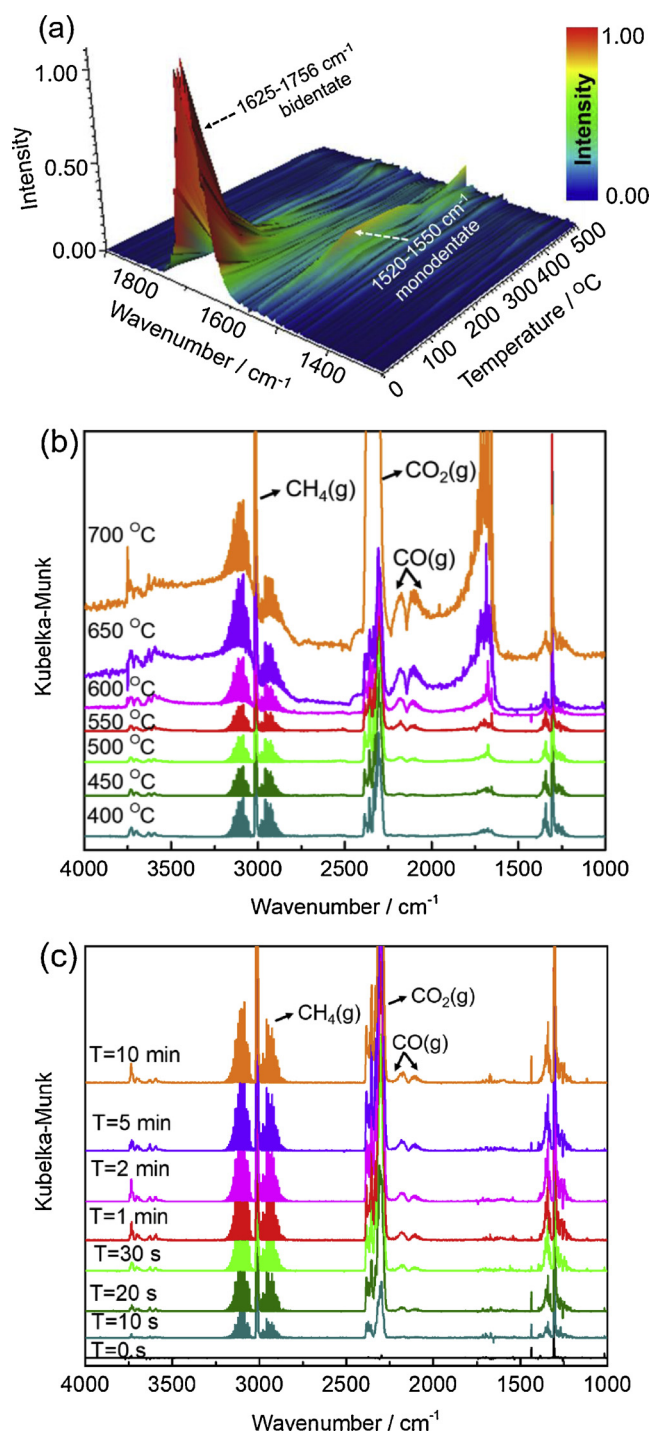
(a)

(b)

(c)

Fig. 9. In situ DRIFTs of (a) CO_2-TPD; (b) MDR reaction at 400–700 °C (CH_4/CO_2/N_2 = 10/10/50 mL/min); and (c) MDR reaction at 500 °C for 10 min (CH_4/CO_2/N_2 = 10/10/50 mL/min) on NiMA-BN-M-R catalyst.

can be attributed to asymmetric deformation vibrations of adsorbed CH_3^*, formates and bidentate carbonates, respectively. The intensity of these characteristic peaks gradually increased along with the reaction time and then stayed constantly after 1 min. At the same time, we can observe that during the proceeding of reaction, −OH peaks gradually appear, which means that the −OH can be generated in the reaction. Combining with the results from Fig. 8, it can prove that during the MDR reaction, the −OH is consumed and regenerated. The appearance of CH_3^* characteristic peaks can further prove that the CH_x^* species were produced during CH_4 activation.
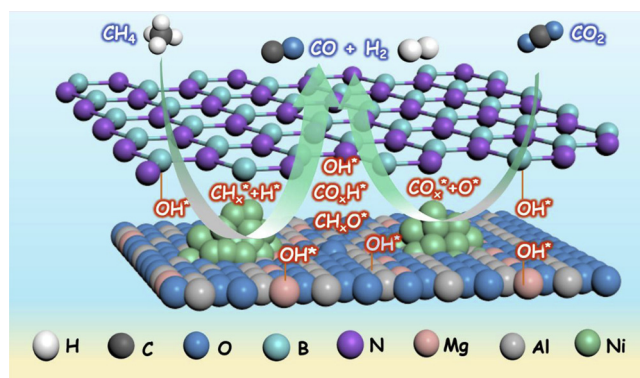

Fig. 10. Possible reaction mechanism over NiMA-BN-M-R catalysts.

Hence, the mechanism for the MDR reaction was proposed in Fig. 10. We conclude that CH_4 could be dissociated on Ni surface to form CH_3^* and H^* species and CO_2 adsorbed on the surface of the carrier forming the carbonate species. Some carbonates species decomposed to formate species and then decomposing to CO. Moreover, the formation of gas-phase CO reveals that RWGS reaction did exist. As it has been mentioned in a previous report, formate can be used as the intermediate for CO formation in the RWGS reaction [57]. Meanwhile, part of the H^* species could combine with the CO_2 to produce formate species which can be further decomposed to produce CO and OH^*. While OH^* can react with the coke on the surface of the catalyst to form CHO^* which then decomposed into CO and H^*. It is beneficial to the elimination of carbon deposit and prevent the deactivation of the catalyst. While, part of the O^* species could combine with the CH_3^* species, thus promoting the decomposition of methane.

4. Conclusion

In summary, we successfully prepared the NiMA-BN-M-R catalyst, in which the confinement strategy can embed the well-dispersed Ni nanoparticles and prevent the sintering of Ni nanoparticles during MDR reaction. The h-BN can improve the thermal stability of the catalyst and hinder the collapse of the $(Ni,Mg)Al_2O_4$ mixed oxide sheets during the high-temperature reaction. At the same time, the SMSI derived from the $Ni/(Ni,Mg)Al_2O_4$ interface can improve the stability of the catalyst. The regenerated NiMA-BN-M-R catalyst showed good stability even after 100 h of the catalyst recycling experiment in MDR reaction. H_2-TPR and TEM analysis demonstrated that the SMSI prevented the sintering of Ni nanoparticles and thus promoting the activation of CH_4. CO_2-TPD and in situ DRIFTs suggested that the strong CO_2 adsorption and activation was observed over the most active catalyst, NiMA-BN-M-R. The fast formation of carbonate and hydroxyl species were beneficial for coke removal during the reaction thus maintaining the good stability of the NiMA-BN-M-R catalyst. Overall, we hope this work can present new clues towards the study of a highly thermal stability composites catalysts for MDR reaction.

Appendix A. Supplementary data

Supplementary material related to this article can be found, in the online version, at doi:https://doi.org/10.1016/j.apcatb.2019.04.007.

References

[1] L.C. Buelens, V.V. Galvita, H. Poelman, C. Detavernier, G.B. Marin, Super-dry reforming of methane intensifies CO_2 utilization via Le Chatelier's principle, Science 354 (2016) 449–452.

[2] A.T. Ashcroft, A.K. Cheetham, M.L.H. Green, P.D.F. Vernon, Partial oxidation of methane to synthesis gas using carbon dioxide, Nature 352 (1991) 225–226.

[3] T. Ryu, N.H. Ahn, S. Seo, J. Cho, H. Kim, D. Jo, G.T. Park, P.S. Kim, C.H. Kim, E.L. Bruce, P.A. Wright, I.S. Nam, S.B. Hong, Fully copper-exchanged high-silica LTA zeolites as unrivaled hydrothermally stable NH_3-SCR catalysts, Angew. Chem. Int. Ed. 129 (2017) 3304–3308.

[4] G.A. Olah, A. Goeppert, M. Czaun, G.K.S. Prakash, Bi-reforming of methane from any source with steam and carbon dioxide exclusively to metgas ($CO-2H_2$) for methanol and hydrocarbon synthesis, J. Am. Chem. Soc. 135 (2013) 648–650.

[5] D. Pakhare, V. Schwartz, V. Abdelsayed, D. Haynes, D. Shekhawat, J. Poston, J. Spivey, Kinetic and mechanistic study of dry (CO_2) reforming of methane over Rh-substituted $La_2Zr_2O_7$ pyrochlores, J. Catal. 316 (2014) 78–92.

[6] S. Dama, S.R. Ghodke, R. Bobade, H.R. Gurav, S. Chilukuri, Active and durable alkaline earth metal substituted perovskite catalysts for dry reforming of methane, Appl. Catal. B: Environ. 224 (2018) 146–158.

[7] M. García-Diéguez, I.S. Pieta, M.C. Herrera, M.A. Larrubia, L.J. Alemany, Nanostructured Pt- and Ni-based catalysts for CO_2-reforming of methane, J. Catal. 270 (2010) 136–145.

[8] I.V. Yentekakis, G. Goula, M. Hatzisymeon, I. Betsi-Argyropoulou, G. Botzolaki, K. Kousi, D.I. Kondarides, M.J. Taylor, C.M.A. Parlett, A. Osatiashtiani, G. Kyriakou, J.P. Holgado, R.M. Lambert, Effect of support oxygen storage capacity on the catalytic performance of Rh nanoparticles for CO_2 reforming of methane, Appl. Catal. B: Environ. 243 (2019) 490–501.

[9] L. Xu, H. Song, L. Chou, One-pot synthesis of ordered mesoporous NiO-CaO-Al2O3 composite oxides for catalyzing CO_2 reforming of CH_4, ACS Catal. 2 (2012) 1331–1342.

[10] J. Lu, B. Fu, M.C. Kung, G. Xiao, J.W. Elam, H.H. Kung, P.C. Stair, Coking- and sintering-resistant palladium catalysts achieved through atomic layer deposition, Science 335 (2012) 1205-1028.

[11] K. Nagaoka, K. Seshan, Ki. Aika, J.A. Lercher, Carbon deposition during carbon dioxide reforming of methane — comparison between Pt/Al_2O_3 and Pt/ZrO_2, J. Catal. 197 (2001) 34–42.

[12] A. Tsoukalou, Q. Imtiaz, S.M. Kim, P.M. Abdala, S. Yoon, C.R. Müller, Dry-reforming of methane over bimetallic Ni-M/La_2O_3 (M = Co, Fe): the effect of the rate of $La_2O_2CO_3$ formation and phase stability on the catalytic activity and stability, J. Catal. 343 (2016) 208–214.

[13] S. Li, J. Gong, Strategies for improving the performance and stability of Ni-based catalysts for reforming reactions, Chem. Soc. Rev. 43 (2014) 7245–7256.

[14] N. Wang, K. Shen, L. Huang, X. Yu, W. Qian, W. Chu, Facile route for synthesizing ordered mesoporous Ni-Ce-Al oxide materials and their catalytic performance for methane dry reforming to hydrogen and syngas, ACS Catal. 3 (2013) 1638–1651.

[15] D. Baudouin, U. Rodemerck, F. Krumeich, Ad. Mallmann, K.C. Szeto, H. Ménard, L. Veyre, J.P. Candy, P.B. Webb, C. Thieuleux, C. Copéret, Particle size effect in the low temperature reforming of methane by carbon dioxide on silica-supported Ni nanoparticles, J. Catal. 297 (2013) 27–34.

[16] J. Arturo Mendoza-Nieto, Y. Duan, H. Pfeiffer, Alkaline zirconates as effective materials for hydrogen production through consecutive carbon dioxide capture and conversion in methane dry reforming, Appl. Catal. B: Environ. 238 (2018) 576–585.

[17] N. Kopfle, T. Gotsch, M. Grunbacher, E.A. Carbonio, M. Havecker, A. Knop-Gericke, L. Schlicker, A. Doran, D. Kober, A. Gurlo, S. Penner, B. Klotzer, Zirconium-assisted activation of palladium boosts syngas production by methane dry reforming, Angew. Chem. Int. Ed. 57 (2018) 14613–14618.

[18] S. Das, J. Ashok, Z. Bian, N. Dewangan, M.H. Wai, Y. Du, A. Borgna, K. Hidajat, S. Kawi, Silica-Ceria sandwiched Ni core-shell catalyst for low temperature dry reforming of biogas: coke resistance and mechanistic insights, Appl. Catal. B: Environ. 230 (2018) 220–236.

[19] M. Li, A.C. van Veen, Tuning the catalytic performance of Ni-catalysed dry reforming of methane and carbon deposition via $Ni-CeO_{2-x}$ interaction, Appl. Catal. B: Environ. 237 (2018) 641–648.

[20] Z. Li, M. Li, Z. Bian, Y. Kathiraser, S. Kawi, Design of highly stable and selective core/yolk-shell nanocatalysts — a review, Appl. Catal. B: Environ. 188 (2016) 324–341.

[21] Y. Cao, P. Maitarad, M. Gao, T. Taketsugu, H. Li, T. Yan, L. Shi, D. Zhang, Defect-induced efficient dry reforming of methane over two-dimensional Ni/h-boron nitride nanosheet catalysts, Appl. Catal. B: Environ. 238 (2018) 51–60.

[22] G. Fan, F. Li, D.G. Evans, X. Duan, Catalytic applications of layered double hydroxides: recent advances and perspectives, Chem. Soc. Rev. 43 (2014) 7040–7066.

[23] J. Xiong, J. Di, J. Xia, W. Zhu, H. Li, Surface defect engineering in 2D nanomaterials for photocatalysis, Adv. Funct. Mater. 0 (2018) 1801983.

[24] L. Wang, J. Zhang, Y. Zhu, S. Xu, C. Wang, C. Bian, X. Meng, F.S. Xiao, Strong metal-support interactions achieved by hydroxide-to-oxide support transformation for preparation of sinter-resistant gold nanoparticle catalysts, ACS Catal. 7 (2017) 7461–7465.

[25] K. Takehira, T. Shishido, P. Wang, T. Kosaka, K. Takaki, Autothermal reforming of CH_4 over supported Ni catalysts prepared from Mg-Al hydrotalcite-like anionic clay, J. Catal. 221 (2004) 43–54.

[26] R. Dębek, M. Motak, M.E. Galvez, T. Grzybek, P. Da Costa, Promotion effect of zirconia on Mg(Ni,Al)O mixed oxides derived from hydrotalcites in CO_2 methane reforming, Appl. Catal. B: Environ. 223 (2018) 36–46.

[27] S. Dai, Z. Fei, Q. Ma, A.S. Rodin, M. Wagner, A.S. McLeod, M.K. Liu, W. Gannett,

[27] W. Regan, K. Watanabe, T. Taniguchi, M. Thiemens, G. Dominguez, A.H.C. Neto, A. Zettl, F. Keilmann, P. Jarillo-Herrero, M.M. Fogler, D.N. Basov, Tunable phonon polaritons in atomically thin van der Waals crystals of boron nitride, Science 343 (2014) 1125–1129.

[28] J.T. Grant, C.A. Carrero, F. Goeltl, J. Venegas, P. Mueller, S.P. Burt, S.E. Specht, W.P. McDermott, A. Chieregato, I. Hermans, Selective oxidative dehydrogenation of propane to propene using boron nitride catalysts, Science 354 (2016) 1570–1573.

[29] L. Gao, Q. Fu, M. Wei, Y. Zhu, Q. Liu, E. Crumlin, Z. Liu, X. Bao, Enhanced nickel-catalyzed methanation confined under hexagonal boron nitride shells, ACS Catal. 6 (2016) 6814–6822.

[30] Y. Cao, M. Lu, J. Fang, L. Shi, D. Zhang, Hexagonal boron nitride supported $mesoSiO_2$-confined Ni catalysts for dry reforming of methane, Chem. Commun. 53 (2017) 7549–7552.

[31] C.Y. Zhi, Y. Bando, T. Terao, C.C. Tang, H. Kuwahara, D. Golberg, Chemically activated boron nitride nanotubes, Chem-Asian J. 4 (2009) 1536–1540.

[32] M. Yu, Y.A. Zhu, Y. Lu, G. Tong, K. Zhu, X. Zhou, The promoting role of Ag in Ni-CeO_2 catalyzed CH_4-CO_2 dry reforming reaction, Appl. Catal. B: Environ. 165 (2015) 43–56.

[33] W. Zhu, X. Gao, Q. Li, H. Li, Y. Chao, M. Li, S.M. Mahurin, H. Li, H. Zhu, S. Dai, Controlled gas exfoliation of boron nitride into few-layered nanosheets, Angew. Chem. Int. Ed. 55 (2016) 10766–10770.

[34] H. Wu, G. Pantaleo, V. La Parola, A.M. Venezia, X. Collard, C. Aprile, L.F. Liotta, Bi- and trimetallic Ni catalysts over Al_2O_3 and Al_2O_3-MO_x (M = Ce or Mg) oxides for methane dry reforming: Au and Pt additive effects, Appl. Catal. B: Environ. 156 (2014) 350–361.

[35] E. le Saché, L. Pastor-Pérez, D. Watson, A. Sepúlveda-Escribano, T.R. Reina, Ni stabilised on inorganic complex structures: superior catalysts for chemical CO_2 recycling via dry reforming of methane, Appl. Catal. B: Environ. 236 (2018) 458–465.

[36] T. Stroud, T.J. Smith, E. Le Sache, J.L. Santos, M.A. Centeno, H. Arellano-Garcia, J.A. Odriozola, T.R. Reina, Chemical CO_2 recycling via dry and bi reforming of methane using $Ni-Sn/Al_2O_3$ and $Ni-Sn/CeO_2-Al_2O_3$ catalysts, Appl. Catal. B: Environ. 224 (2018) 125–135.

[37] K. Jabbour, P. Massiani, A. Davidson, S. Casale, N. El Hassan, Ordered mesoporous "one-pot" synthesized Ni-Mg(Ca)-Al_2O_3 as effective and remarkably stable catalysts for combined steam and dry reforming of methane (CSDRM), Appl. Catal. B: Environ. 201 (2017) 527–542.

[38] S. Damyanova, B. Pawelec, R. Palcheva, Y. Karakirova, M.C. Capel Sanchez, G. Tyuliev, E. Gaigneaux, J.L.G. Fierro, Structure and surface properties of ceria-modified Ni-based catalysts for hydrogen production, Appl. Catal. B: Environ. 225 (2018) 340–353.

[39] M. Gil-Calvo, C. Jiménez-González, B. de Rivas, J.I. Gutiérrez-Ortiz, R. López-Fonseca, Effect of Ni/Al molar ratio on the performance of substoichiometric $NiAl_2O_4$ spinel-based catalysts for partial oxidation of methane, Appl. Catal. B: Environ. 209 (2017) 128–138.

[40] R.C. Rabelo-Neto, H.B.E. Sales, C.V.M. Inocencio, E. Varga, A. Oszko, A. Erdohelyi, F.B. Noronha, L.V. Mattos, CO_2 reforming of methane over supported $LaNiO_3$ perovskite-type oxides, Appl. Catal. B: Environ. 221 (2018) 349–361.

[41] L. Pino, C. Italiano, A. Vita, M. Lagana, V. Recupero, $Ce_{0.70}La_{0.20}Ni_{0.10}O_2$-delta catalyst for methane dry reforming: influence of reduction temperature on the catalytic activity and stability, Appl. Catal. B: Environ. 218 (2017) 779–792.

[42] D. Harshini, D.H. Lee, J. Jeong, Y. Kim, S.W. Nam, H.C. Ham, J.H. Han, T.H. Lim, C.W. Yoon, Enhanced oxygen storage capacity of $Ce_{0.65}Hf_{0.25}M_{0.1}O_{2-δ}$ (M = rare earth elements): applications to methane steam reforming with high coking resistance, Appl. Catal. B: Environ. 148-149 (2014) 415–423.

[43] A.G. Bhavani, W.Y. Kim, J.S. Lee, Barium substituted lanthanum manganite perovskite for CO_2 reforming of methane, ACS Catal. 3 (2013) 1537–1544.

[44] D. Li, R. Li, M. Lu, X. Lin, Y. Zhan, L. Jiang, Carbon dioxide reforming of methane over Ru catalysts supported on Mg-Al oxides: a highly dispersed and stable Ru/Mg(Al)O catalyst, Appl. Catal. B: Environ. 200 (2017) 566–577.

[45] S.D. Angeli, L. Turchetti, G. Monteleone, A.A. Lemonidou, Catalyst development for steam reforming of methane and model biogas at low temperature, Appl. Catal. B: Environ. 181 (2016) 34–46.

[46] S. Zhang, S. Muratsugu, N. Ishiguro, M. Tada, Ceria-doped Ni/SBA-16 catalysts for dry reforming of methane, ACS Catal. 3 (2013) 1855–1864.

[47] F. Wang, B. Han, L. Zhang, L. Xu, H. Yu, W. Shi, CO_2 reforming with methane over small-sized Ni@SiO_2 catalysts with unique features of sintering-free and low carbon, Appl. Catal. B: Environ. 235 (2018) 26–35.

[48] F. Polo-Garzon, M. He, D.A. Bruce, Ab initio derived reaction mechanism for the dry reforming of methane on Rh doped pyrochlore catalysts, J. Catal. 333 (2016) 59–70.

[49] N. Wang, K. Shen, L. Huang, X. Yu, W. Qian, W. Chu, Facile Route for Synthesizing Ordered Mesoporous Ni-Ce-Al Oxide Materials and Their Catalytic Performance for Methane Dry Reforming to Hydrogen and Syngas, ACS Catal. 3 (2013) 1638–1651.

[50] J.W. Han, C. Kim, J.S. Park, H. Lee, Highly coke-resistant Ni nanoparticle catalysts with minimal sintering in dry reforming of methane, Chemsuschem 7 (2014) 451–456.

[51] S.A. Theofanidis, R. Batchu, V.V. Galvita, H. Poelman, G.B. Marin, Carbon gasification from Fe-Ni catalysts after methane dry reforming, Appl. Catal. B: Environ. 185 (2016) 42–55.

[52] M.M. Nair, S. Kaliaguine, F. Kleitz, Nanocast $LaNiO_3$ perovskites as precursors for the preparation of coke-resistant dry reforming catalysts, ACS Catal. 4 (2014) 3837–3846.

[53] T. Jawhari, A. Roid, J. Casado, Raman spectroscopic characterization of some commercially available carbon black materials, Carbon 33 (1995) 1561–1565.

[54] F.C. Meunier, D. Reid, A. Goguet, S. Shekhtman, C. Hardacre, R. Burch, W. Deng, M. Flytzani-Stephanopoulos, Quantitative analysis of the reactivity of formate

species seen by DRIFTS over a Au/Ce(La)O$_2$ water-gas shift catalyst: first un-ambiguous evidence of the minority role of formates as reaction intermediates, J. Catal. 247 (2007) 277–287.

[55] K. Li, F. He, H. Yu, Y. Wang, Z. Wu, Theoretical study on the reaction mechanism of carbon dioxide reforming of methane on La and La$_2$O$_3$ modified Ni(111) surface, J. Catal. 364 (2018) 248–261.

[56] G. Busca, V. Lorenzelli, Infrared spectroscopic identification of species arising from reactive adsorption of carbon oxides on metal oxide surfaces, Mater. Chem. 7 (1982) 89–126.

[57] L.F. Bobadilla, V. Garcilaso, M.A. Centeno, J.A. Odriozola, Monitoring the reaction mechanism in model biogas reforming by in situ transient and steady-state DRIFTS measurements, ChemSusChem 10 (2017) 1193–1201.

[58] Y. Wang, L. Yao, Y. Wang, S. Wang, Q. Zhao, D. Mao, C. Hu, Low-temperature catalytic CO$_2$ dry reforming of methane on Ni-Si/ZrO$_2$ catalyst, ACS Catal. 8 (2018) 6495–6506.

[59] X.L. Yan, T. Hu, P. Liu, S. Li, B.R. Zhao, Q. Zhang, W.Y. Jiao, S. Chen, P.F. Wang, J.J. Lu, L.M. Fan, X.N. Deng, Y.X. Pan, Highly efficient and stable Ni/CeO$_2$-SiO$_2$ catalyst for dry reforming of methane: effect of interfacial structure of Ni/CeO$_2$ on SiO$_2$, Appl. Catal. B: Environ. 246 (2019) 221–231.